Journal of Materials Chemistry C

ROYAL SOCIETY OF CHEMISTRY

PAPER

View Article Online
View Journal

Cite this: DOI: 10.1039/d5tc02913a

Employing Eu,Tb-doped HfO_2 nanocrystals as built-in cryogenic luminescent nanothermometers for commercial coated conductors

Pauline Rooms,[a] Mirijam Lederer,[b] Ian Pompermayer Machado,[b] Martina Tsvetanova,[c] Klaartje De Buysser,[a] Anna M. Kaczmarek *[b] and Hannes Rijckaert[a]

Received 1st August 2025,
Accepted 12th December 2025

DOI: 10.1039/d5tc02913a

rsc.li/materials-c

This work presents a novel approach for detecting quench or hot spot regimes in coated conductors by depositing luminescent nanocrystals operating as nanothermometers onto the silver protective layer, allowing simultaneous temperature measurements. In this work, we use hafnium oxide (HfO_2) nanocrystals doped with Eu^{3+} and Tb^{3+} ions, synthesized *via* a microwave-assisted solvothermal method, which were next spin-coated onto the protective layer of coated conductor tape. HfO_2:4.5%Eu^{3+},0.5%Tb^{3+} nanocrystals exhibited a relative sensitivity of up to 4.10% K^{-1} at 40 K. The nanocrystal-derived thin film, with a thickness of 60 ± 10 nm, exhibited good thermometric performance, with a relative sensitivity of 13.51% K^{-1} at 20 K. It also retained the superconducting properties of the coated conductor.

Introduction

High-temperature superconducting (HTS) tape based on REBCO ($REBa_2Cu_3O_{7-x}$, where RE stands for rare-earth) coated conductors is promising for electrical applications and can additionally help to reduce energy losses and enable new carbon-free energy sources, mitigating negative impacts on the climate.[1,2] However, a problem associated with reliable continuous operation of HTS applications is the behavior of the conductor when part of it reverts from the superconducting state back to its normal conducting state due to disturbances in the superconducting layer.[3–5] This phenomenon is called a quench or hot spot regime, and it can be caused by local damage in the superconducting layer that induces excessive local temperatures and non-uniform current density distribution in the film. After a quench, a normal conducting zone with finite resistance forms in the superconducting tape, dissipating energy through Joule heating. This zone spreads along the superconducting layer due to the low thermal conductivity (W m^{-1} K^{-1}) and high specific heat capacity (J kg^{-1} K^{-1}). The speed of this propagation is referred to as the normal zone propagation velocity (NZPV).[6–9] This NZPV plays a crucial role in the thermal stability and is typically expressed in meters per second (in the m s^{-1} range) for low-temperature superconductors (LTS) or centimeters per second (in the cm s^{-1} range) for HTS.

A low NZPV concentrates the local joule heating within a small section of the tape, leading to irreversible damage (even rupturing the cross-section of the superconducting tape completely), while a higher NZPV allows for effective heat dissipation over an extended surface across a large normal zone.[10] Therefore, understanding, monitoring, and controlling the NZPV is crucial to prevent local overheating and potential damage to the superconducting tape.[5,11,12] It is then necessary to implement protective measures such as quench detection systems. Most quench detection technologies are capable of detecting NZPV at speeds in the range of m s^{-1}. However, detecting NZPV on a cm s^{-1} magnitude, while simultaneously preventing quench propagation, remains a challenge.[8] Several types of quench detection have been proposed, including methods based on temperature,[7] magneto-optical effects,[13] voltage,[14] pressure,[15] fluorescence,[16] and Rayleigh scattering.[17] Each approach has its own advantages and limitations. In this work, we focused on temperature-based quench detection as it is extremely useful to develop a new quench detection method capable of monitoring the temperature of the HTS tape with high resolution and good sensitivity of the temperature measurements, conducted over a large area. Additionally, a fast temperature readout that is not affected by the substrate is of high importance to ensure correct and accurate temperature readout.

For those requirements, conventional contact thermometry methods, such as thermocouples, are unsuitable for monitoring

[a] SCRiPTS, Department of Chemistry, Ghent University, Krijgslaan 289-S3, 9000 Ghent, Belgium
[b] NanoSensing Group, Department of Chemistry, Ghent University, Krijgslaan 289-S3, 9000 Ghent, Belgium. E-mail: Anna.Kaczmarek@UGent.be
[c] MESA+ Institute for Nanotechnology, Faculty of Electrical Engineering, Mathematics and Computer Science, University of Twente, Enschede 7500 AE, Netherlands

temperature due to their low spatial and thermal resolution, as well as low spatial and thermal sensitivity.[18–20] More importantly, their invasive characteristics can disrupt the superconductor system. Non-contact methods like infrared (IR) thermography, Raman spectroscopy, and luminescence-based thermometry have certain advantages such as their higher spatial and thermal resolution.[21,22] However, IR thermometry is limited to surface temperature measurements and lacks in-depth information, while Raman spectroscopy suffers from low signal levels and potential interference with fluorescent molecules inside the sample. Luminescent thermometry has gained significant interest due to its minimally invasive and non-destructive characteristics, remote access, high thermal and spatial resolution together with high sensitivity. Lanthanide (Ln)-based materials are some of the most promising candidates for use as luminescent thermometers. The ratiometric approach is one of the simplest methods, which utilizes the intensity ratio between two emission bands.[18,23] This approach relies on temperature-dependent changes of the luminescence emissions in steady state mode, comparing the ratios of the peaks to each other. If the two electronic states are thermally coupled, a Boltzmann distribution is fitted to achieve a primary thermometer. This approach is less dependent on background, experimental conditions, and the environment and therefore less prone to errors in readout, inaccuracies and uncertainty as it has an internal reference.[24–26]

Here, ratiometric luminescence thermometry based on Ln^{3+}-doped nanomaterials can provide an effective solution for detecting quench or hot spot regimes on superconducting materials with cm s^{-1} magnitude. The host material for Ln-based thermometry should exhibit good crystallinity, which is essential for Ln^{3+} ions as their intraconfigurational 4f–4f transitions require good crystallinity to achieve high-intensity emissions. Highly crystalline metal oxide thin films are often obtained by thermal treatment under controlled oxygen partial pressure during or after deposition. Nevertheless, the thermal budget of the coated conductor must be carefully considered, as treatments at elevated temperatures (above 600 °C) can deform, delaminate, or oxidize the substrate, or even degrade the superconducting layer in an oxygen-rich atmosphere.[27] Furthermore, it should be noted that the thickness of the thermometer layer, when applied as a thin film coating in the multi-stacked architecture of the coated conductor, must be minimized to avoid compromising the engineering critical current density, while still ensuring high signal intensity and reliable thermometric performance. As a thin film, nanothermometers can be integrated into the coated conductor architecture for localized temperature sensing. In this context, nanoparticle-derived thin films are advantageous because the nanoparticles with the desired crystallinity and luminescence properties can be previously synthesized and later simply deposited onto the desired substrate at room temperature (RT). However, size-dependent luminescence quenching and its negative influence on thermal sensitivity are known issues in nanothermometry,[28] making it challenging to balance the benefits and drawbacks of small nanoparticle sizes. Choosing a host material for a lanthanide-based nanothermometer can be particularly difficult, especially when the host material not only serves as a dopant embedding medium but also exhibits its own luminescent properties, as was the case in this study.[21]

In this work, hafnium oxide (HfO_2) was chosen as the host material for lanthanide luminescence-based thermometry, as it is optically transparent and offers high chemical, mechanical and thermal stability in all temperature regions, from the cryogenic region to very high temperatures.[29] Despite the fact that organic/hybrid host matrices with lanthanides (Eu–Tb) exhibit orders-of-magnitude higher luminescence intensity at cryogenic temperatures,[30–33] they cannot be incorporated into coated conductor architectures due to several reasons, such as the lack of long-term stability and the limited flexibility (due to the rigidity) of metal–organic frameworks (MOFs) and other organic-based materials. Also, high crystallinity of the host material is crucial since the crystal field symmetry and strength affects the 4f–4f electronic transitions, which are only partially allowed by the forced electric dipole mechanism due to asymmetries in the crystal field of centrosymmetric crystals.[34,35] Increasingly complex thermometric systems are being developed by incorporating nanoparticles into various devices and compounds, aiming to combine their strengths and reduce their weaknesses, with applications in fields such as catalysis and microelectronics.[36–39] Other emerging applications of lanthanide-based luminescent thermometry are often found in the (bio)medical field such as *in vivo* luminescent thermometry for deep-tissue temperature imaging and intratumoral thermal monitoring during photo-therapy.[40,41] Despite the above-mentioned qualities, only a few studies have reported HfO_2 as a host material for lanthanide luminescence-based thermometry (hereafter referred to as thermometry).[33,42,43] In this work, HfO_2:Eu^{3+},Tb^{3+} nanocrystals are synthesized and characterized for thermometric application, achieved by depositing the luminescent nanocrystals as a thin film onto the silver protective layer of coated conductors (Fig. 1). Previous studies, including some of our own, have demonstrated that Tb–Eu systems are highly suitable for developing thermometers in the cryogenic region due to their excellent relative sensitivities.[33,44] To the best of our knowledge,

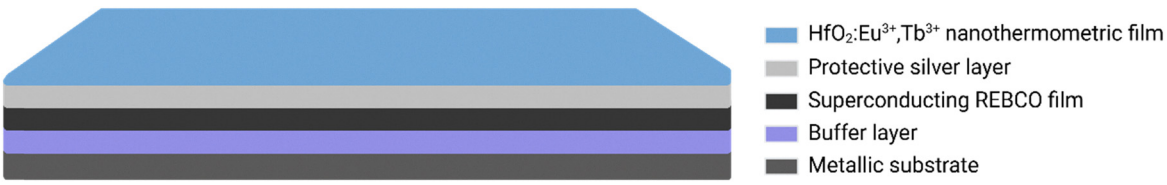

Fig. 1 Schematic representation of the cross-sectional view of the coated REBCO conductor with a HfO_2:Eu^{3+},Tb^{3+} nanothermometric film on top of the protective silver layer.

this is the first report of a combined nanothermometer-superconductor system. The integrated system exhibits excellent luminescence thermometric behavior at cryogenic temperatures while preserving its superconducting properties.

To demonstrate the feasibility of applying this nanothermometry approach under cryogenic conditions, a conceptual implementation is proposed for *in situ* temperature monitoring. As nanothermometry is an optical and remote sensing technique, relying on photon excitation and consequent emission detection, the setup requires integrating a readout system properly aligned with the nanothermometric film. For practical implementations, such as temperature monitoring of a superconducting magnet, only the cross-sectional area of the thermometry film is exposed and the luminescent probe must be in direct physical contact with the material being measured, even though excitation and emission are detected optically. Consequently, precise control over film thickness and uniformity is essential to achieve reliable and reproducible measurements. Therefore, the superconductors' geometry and accessibility must be considered when building a detection system around it, to offer reproducibility, minimize artifacts, and enable precise and intense signal detection. It should be noted that, while the system as presented does not yet demonstrate the detection of localized hot spots or resolve NZPV, this limitation is acceptable within the scope of the current proof-of-concept study. These limitations arise from the combination of nanocrystal luminescence behavior at cryogenic temperatures and practical constraints in optical alignment and thin-film uniformity. These factors reduce spatial resolution and sensitivity at cryogenic temperatures, potentially affecting the detection of localized hot spots and NZPV. Currently, the proposed proof-of-concept system shows good thermometric parameters. Further work will focus on lab-scale tape sections to: (1) deposit and optimize nanothermometric films on operational superconducting tape, (2) optimize excitation/emission and optical readout to improve collection efficiency and spatial resolution, and (3) benchmark against conventional cryogenic thermometry to validate performance under realistic superconducting and magnetic conditions. Subsequently, the system can be gradually integrated into larger devices for scaling real superconducting applications, ensuring reproducible and accurate temperature monitoring. By proposing a feasible integration strategy and addressing practical limitations, this study demonstrates potential for real-world applications rather than serving solely as a conceptual demonstration.

Experimental section

Materials

Unless specified otherwise, all manipulations were conducted in ambient air. Hafnium(IV) chloride ($HfCl_4$, 98%), hydrochloric acid (HCl, 37%), and terbium(III) acetate hydrate ($Tb(ace)_3$, 99.9%) were purchased from Sigma-Aldrich. Europium(III) acetate hydrate ($Eu(ace)_3$, 99.9%) was purchased from Thermo Scientific Chemicals. Tetrahydrofuran (THF, ExtraDry, 99.5%) and dichloromethane (DCM, anhydrous 99.6%) were purchased from Acros Organics. Oleic acid (90% technical grade) was purchased from VWR. Solvents used for synthesis were purchased from Chem-Lab. Benzyl alcohol (BnOH, ReagentPlus® ≥ 99%) was vacuum distilled and stored over sieves based on a method of Horton *et al.*[45] Oleyl amine (70%) was purified according to Baranov *et al.*[46] Both were purchased from Sigma-Aldrich. The YBCO coated conductor tape was taken from the standard production of Deutsche Nanoschicht GmbH (D-Nano, Germany). This was all-chemical-based tape that consisted of 10 mm wide and 60 μm thick Ni-5 at% W alloy RABiTS (99% Cube within 15° misorientation) coated with $La_2Zr_2O_7$ buffer, CeO_2 buffer, YBCO superconducting, and Ag protective layers.[47]

HfO_2:Eu^{3+},Tb^{3+} nanocrystal synthesis procedures

The synthesis of undoped HfO_2 nanocrystals has been previously described by Goossens *et al.*,[48] where the precursor hafnium(IV) chloride tetrahydrofuran complex ($HfCl_4$·2THF) was first adapted from the procedure of Manxzer *et al.*[49] and subsequently optimized. Briefly, 0.069 mol $HfCl_4$ is partly dissolved in 220 mL DCM and is completely dissolved when THF is added in a dropwise manner, forming crystals after a few minutes. The solution is frozen, filtered, and washed with pentane, resulting in a white $HfCl_4$·2THF powder. The HfO_2 nanocrystal synthesis is based on the original solvothermal synthesis by Buha *et al.*[50] which was later adapted into a microwave-assisted synthesis by De Roo *et al.*[51] This was further optimized by Goossens *et al.*[48] through the use of the $HfCl_4$·2THF complex. To adapt this synthesis towards the HfO_2:Eu^{3+},Tb^{3+} nanocrystals, $Tb(ace)_3{\cdot}xH_2O$ and $Eu(ace)_3{\cdot}xH_2O$ were predissolved in 4 mL of BnOH and 0.6 mmol $HfCl_4$·2THF was added to the BnOH mixture and transferred into a 10 mL glass microwave vial. This mixture was subjected to microwave radiation at 220 °C for 4 hours in CEM Discover SP microwave equipment (infrared temperature control) with medium stirring provided by a magnetic Teflon stirrer. After microwave-assisted synthesis, the reaction mixture was transferred to a centrifuge tube and rinsed with 3 mL of diethyl ether. After mild centrifugation (720 rcf, 2 min), three phases were observed: the transparent organic (top) phase, the aqueous milky (middle) phase, and the solid (bottom) phase. The top phase was removed by pipetting, and the milky phase was separated from the solid phase by decantation. Ethanol was then added to the milky phase, yielding 2 mL of a transparent nanosuspension. This nanosuspension was precipitated by the addition of 5 mL of diethyl ether. After centrifugation (4500 rcf, 2 min), the HfO_2 nanocrystals capped with HCl, were post-functionalized with 50 μL of oleic acid and 50 μL of oleyl amine, yielding a clear suspension in 4 mL of toluene. For some measurements, ligand-free nanocrystals were used. To obtain ligand-free nanocrystals, the nanocrystals were dispersed in 1 mL of toluene. HCl was added until the solution reached a pH of approximately 3–4 (1 or 2 drops of 1 M HCl). Then, 1 mL of distilled water was added, and the mixture was sonicated for 1 hour at RT. Afterwards, the nanocrystals were washed with a 1 : 20 volume ratio of ethanol and then with distilled water (centrifuge settings: 4 minutes at 7000 rcf). The resulting powder was dried overnight in a drying furnace at 80 °C.

Characterization of HfO_2 nanocrystals

Transmission electron microscopy (TEM) images of undoped and doped HfO_2 nanocrystals were taken with a JEOL JEM1010 TEM without Cs correction (TEM Core Facility of Ghent University, operated at 100 kV). The samples were prepared by placing 1 or 2 drops of diluted nanocrystals suspension onto a 300-mesh holey carbon copper grid and letting it air-dry at RT. The average size of the nanocrystals was obtained using the open-source software ImageJ. Thermo Scientific Spectra 300 TEM at the University of Twente, operated at an acceleration voltage of 300 kV and equipped with a Super-X G2 energy-dispersive X-ray spectroscopy (EDX) detector, was used in high-angle annular dark-field (HAADF) mode to analyze the chemical composition of doped HfO_2 nanocrystals.

The crystallinity of the nanocrystals was determined *via* powder X-ray diffraction (PXRD) using a Bruker D8 Advance diffractometer operated using the Bragg–Brentano θ–2θ geometry (goniometer radius of 280 mm) and Cu-Kα radiation (λ = 1.54184 Å). No Kβ filter was applied. The detector is a LynxEye XE-T Silicon strip Line detector with 192 channels. The sample was prepared by dropping and drying 50 µL of the nanosuspension onto a glass substrate. Energy Dispersive X-ray Fluorescence (XRF) spectroscopy was used to determine the actual composition of the doped HfO_2 nanocrystals. This was performed with a Rigaku NEX CG Spectrometer on filter paper, onto which 10 drops of nanosuspension were applied and air-dried. The Rigaku NEX CG works with a close-coupled Cartesian Geometry under helium flow and is equipped with a palladium anode X-ray tube and silicon drift detector.

Deposition and characterization of the HfO_2:Eu^{3+},Tb^{3+} film

First, the commercial YBCO tape underwent ultrasonic cleaning in isopropanol for 10 minutes, followed by heating on a hotplate at 120 °C in an ambient atmosphere to remove solvent residues. A doped HfO_2:Eu^{3+},Tb^{3+} nanocrystal suspension, with toluene as the solvent and a concentration of 0.15 mol L^{-1} was spin-coated five times onto the cleaned YBCO tape at a spin speed of 34 rps for 60 seconds using a KLM SCC-200 model. Subsequently, the wet coating was dried at 130 °C on the hotplate in an ambient atmosphere for 5 minutes. Scanning TEM images of thin films were captured using a JEOL JEM-2200FS TEM at Ghent University TEM core facility, operated at 200 kV with a bright field (BF) detector. For the STEM measurements, a cross-sectional TEM lamella was prepared based on a technical note.[52] The self-field critical current densities J_c of the YBCO thin films at 77 K were measured inductively with an electric field criterion of 50 µV cm^{-1} with a CryoScan (THEVA GmbH).

Photoluminescence of HfO_2:Eu^{3+},Tb^{3+} nanocrystals

Photoluminescence spectra were recorded on an Edinburgh Instruments FLSP 920 UV-vis-NIR spectrometry set-up with a 450 W xenon lamp as the steady-state excitation source. The data were collected either in suspension, as dried powder or as thin films. The colloidal suspensions of the nanocrystals dispersed in toluene were measured in a 3 mL quartz cuvette with a 10 mm path length. Luminescence decay times were recorded using a 60 W pulsed xenon lamp, operating at a frequency of 100 Hz. Cryostat measurements were performed in powder or on the thin films in a closed cycle cryostat from Advanced Research Systems, United States. The spectra were recorded in the range of λ = 400–750 nm and at temperatures ranging from 20 to 100 K, using steps of 10 K. These measurements were carried out on ligand-free nanocrystals. All thermometric calculations were performed using TeSen software.[53]

Results and discussion

The microwave-assisted synthesis of both undoped HfO_2 and doped HfO_2:Eu^{3+},Tb^{3+} nanocrystals yields ellipsoidal-shaped nanocrystals, as shown in the TEM images (Fig. 2(a) and (b)). The corresponding histograms (Fig. 2(b)) reveal an average

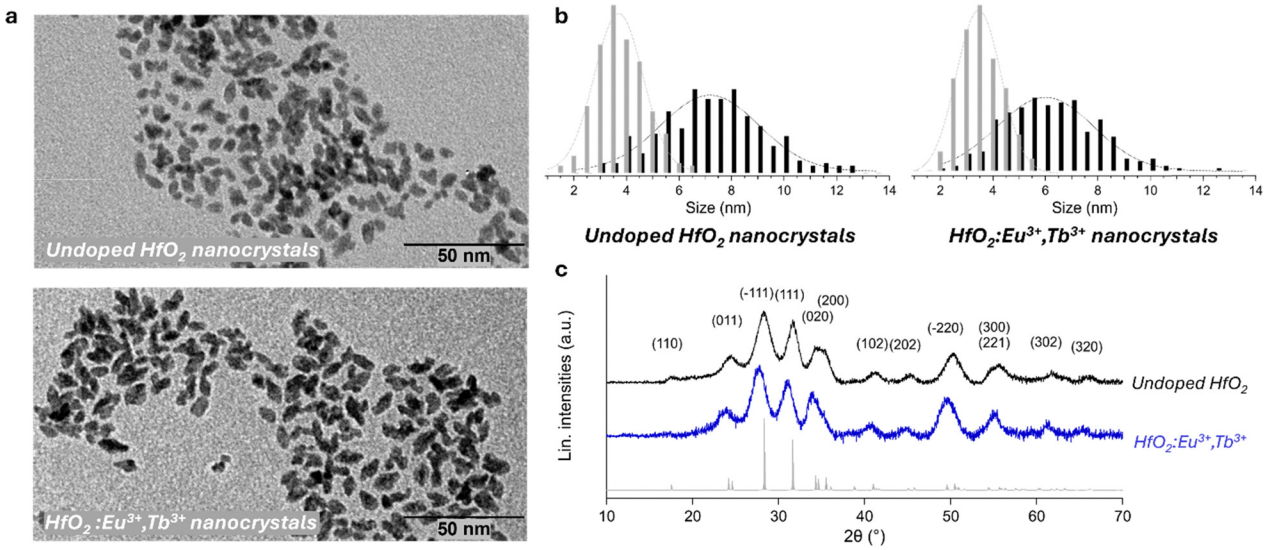

Fig. 2 Undoped HfO_2 and HfO_2:4.5%Eu^{3+},0.5%Tb^{3+} nanocrystals after the microwave-assisted synthesis: (a) TEM images, (b) TEM histograms and (c) PXRD patterns, indexing of peaks is based on the data from the standard JCPDS file (ICSD-60902).

long-axis length of 7.5 ± 5.9 nm and a short-axis length of 4.0 ± 2.8 nm ($\mu \pm 3\sigma$) for the undoped HfO_2. The PXRD patterns, shown in Fig. 2(c), confirm good crystallinity and the monoclinic crystal structure, matching the monoclinic HfO_2 ($P12_1/c1$) reference data (ICSD-60902). Therefore, these parameters were assessed for HfO_2 nanocrystals doped with 4.5%Eu and 0.5%Tb, as shown in Fig. 2(a–c), resulting in nanocrystals with a long-axis length of 6.4 ± 5.3 nm and short-axis length of 3.8 ± 2.3 nm ($\mu \pm 3\sigma$) and monoclinic phase. However, it is well-known that doping nanocrystals, particularly at high concentrations of dopants, can change the crystallinity, morphology, and properties of nanocrystals, as demonstrated in a study by Lauria *et al.*[29] In our work, these results indicate that a total of 5% aliovalent Ln^{3+}-doping does not significantly affect the size, morphology, or crystallinity of the HfO_2 nanocrystals.

HfO_2:4.5%Eu^{3+},0.5%Tb^{3+} nanocrystals were selected for photoluminescence thermometry studies (RT excitation and emission spectra are shown in Fig. 3) based on preliminary assessment of different Eu/Tb dopant ratios in HfO_2 nanocrystals at RT. A compact overview of the doping ratio optimization process can be found in the SI (Fig. S1 and S2 and Tables S1 and S2). The effective dopant concentrations of Eu and Tb ions in HfO_2 nanocrystals were determined using XRF spectroscopy to verify that the expected doping percentages were achieved. The effective concentrations deviated slightly from the nominal values: 3 mol% Eu instead of the expected 4.5 mol% and 1 mol% Tb instead of 0.5 mol%. These variations are expected and fall within the tolerated limits. The nanocrystals with this ratio will hereafter be referred to as HfO_2:Eu^{3+},Tb^{3+} nanocrystals in this work. However, the final confirmation of the incorporation of Eu and Tb ions into the HfO_2 nanocrystals is provided by the EDX compositional mapping (Fig. 4(a) and Fig. S3 in the SI). The EDX spectrum (Fig. 4(b)) shows the presence of Eu M (1.131 keV) and Tb M (1.240 keV) peaks, confirming that the ions are incorporated into the HfO_2 lattice rather than segregated at the surface or forming secondary phases.

Examples of luminescence thermometers based on the Tb–Eu ion pair are well known and usually perform especially well in the cryogenic temperature range. Some important works are mentioned in the references herein.[31,54–56] To evaluate the thermometric performance of the HfO_2:Eu^{3+},Tb^{3+} nanocrystals, four thermometric parameters were used: the thermometric parameter Delta (Δ), the relative sensitivity (S_r), the temperature uncertainty (σT) and repeatability (R).[42] These parameters were calculated and plotted using TeSen software,[53] using equations shown below. The luminescence intensity ratio Δ between the two relevant emission peaks was calculated by dividing the integrated areas under each peak. Two combinations of emission peaks were selected for the Δ calculations: Tb^{3+}/Eu^{3+} and HfO_2 (host emission)/Eu^{3+}. The experimental Δ points were fitted using the polynomial fit (eqn (1)). Depending on the degree of polynomial fit, a different number of terms are used to achieve a satisfactory goodness of fit.

$$\Delta_p = \Delta_0 + \Delta_1(T - T_0) + \Delta_2(T - T_0)^2 + \ldots \quad (1)$$

$$S_r = 100\% \times \left|\frac{1}{\Delta}\frac{\partial \Delta}{\partial T}\right| \quad (2)$$

The S_r indicates the maximum relative sensitivity, the relative change of thermometric parameter per degree of temperature change and is expressed in % K^{-1} (eqn (2)).[57]

$$\sigma T = \frac{1}{S_r}\sqrt{\frac{1}{I_1} + \frac{1}{I_2}} \quad (3)$$

The temperature uncertainty σT (eqn (3)) measures the smallest temperature variation (in K) a certain luminescent thermometer can detect, thus being an essential parameter to assess the thermometric performance of a given system. To evaluate whether the material can reliably function as a thermometer for multiple uses, it is important to perform cycle tests. The repeatability is then quantified using eqn (4). In this equation, Δ_c is the average value of thermometric parameter, and Δ_i refers to the individual measurement values of the thermometric parameter. This formula helps assess how consistent the measurements are across different cycles. Our material showed a repeatability of 98% (Fig. S4).

$$R = 1 - \frac{\max|\Delta_c - \Delta_i|}{\Delta_c} \quad (4)$$

In several earlier works, it was shown that a weak Tb^{3+} emission and a strong Eu^{3+} emission is favorable for cryogenic

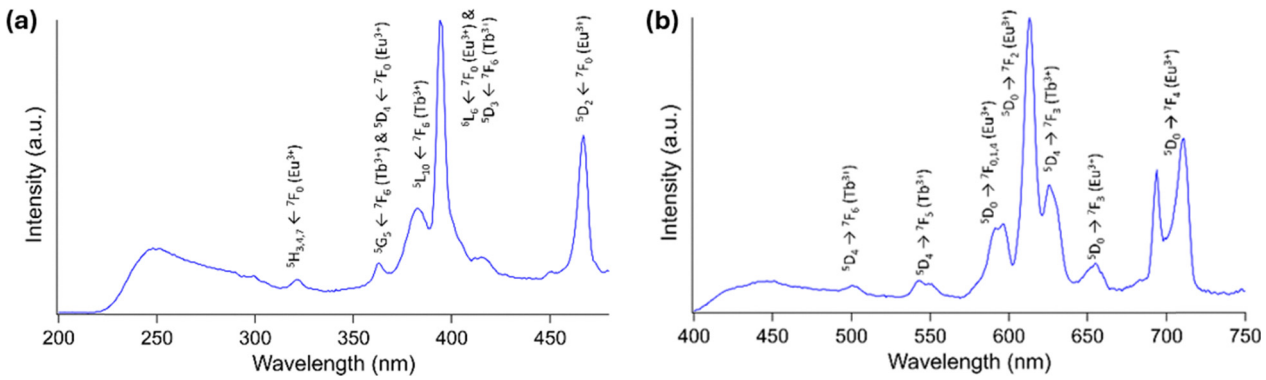

Fig. 3 Photoluminescence spectra of HfO_2:Eu^{3+},Tb^{3+} nanocrystals measured at RT as a powder in the cryostat: (a) excitation spectrum (λ_{em} = 613 nm), and (b) emission spectrum (λ_{ex} = 250 nm).

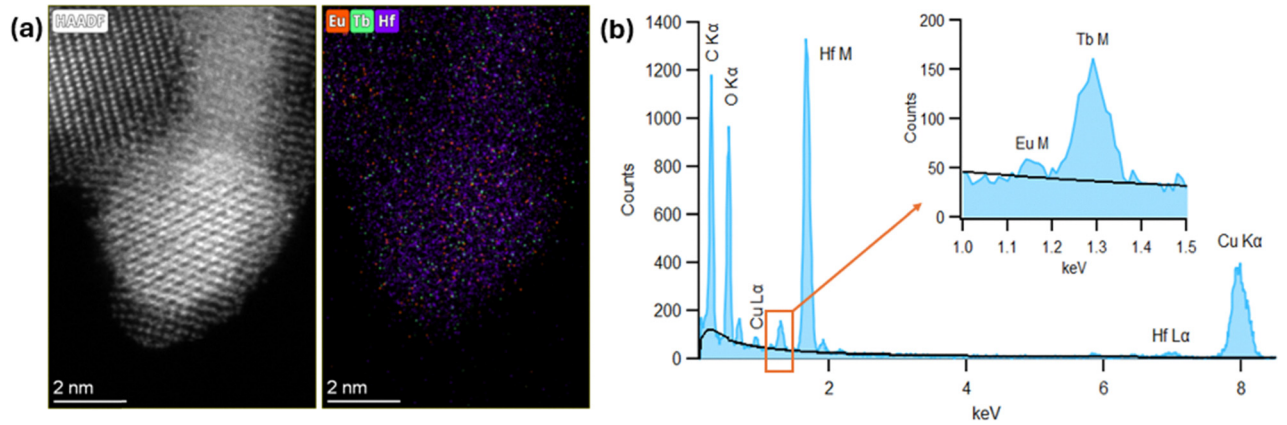

Fig. 4 (a) HAADF-STEM image with corresponding EDX compositional maps and (b) spectrum showing the presence of Eu^{3+} and Tb^{3+} ions in the HfO_2 nanocrystal core. The black curve in the EDX spectrum represents the background signal.

thermometry.[32,33] The thermometric properties of the HfO_2:Eu^{3+},Tb^{3+} nanocrystals were evaluated by carrying out measurements in the cryogenic region (20 K to 100 K with a step size of 10 K). As the first two data points (20 K and 30 K) did not yield monotonic behavior, therefore only the 40–100 K range was taken into account for calculations. Fig. 5 shows the emission map (a), the intensities of the 545 nm ($^5D_4 \rightarrow {}^7F_5$ electronic transition of Tb^{3+}) and 613 nm peak ($^5D_0 \rightarrow {}^7F_2$ electronic transition of Eu^{3+}) (b), as well as the intensities of the 400–550 nm broadband originating from the HfO_2 host material and the 613 nm peak ($^5D_0 \rightarrow {}^7F_2$ electronic transition of Eu^{3+}) (c). Fig. 5(d)–(f) show the respective Δ, S_r, and σT thermometric parameters, calculated based on the integrated areas under the Tb^{3+} $^5D_4 \rightarrow {}^7F_5$ and Eu^{3+} $^5D_0 \rightarrow {}^7F_2$ transitions. It should be noted that the $^5D_4 \rightarrow {}^7F_5$ transition peak of Tb^{3+} overlaps with the emission of the HfO_2 host. For the purpose of calculations, we did not separate a baseline for the $^5D_4 \rightarrow {}^7F_5$ transition peak, and therefore its thermometric behavior is to some degree dependent on the thermometric behavior of the HfO_2 host material. The relative sensitivity S_r reached a maximum of 4.10% K^{-1} at 40 K and a very good temperature uncertainty throughout the whole studied temperature range $\sigma T < 0.09$ K. Additionally to these transitions, the broad emission band of the HfO_2 host is strong at cryogenic temperatures and can thus also be used for ratiometric thermometry with the 613 nm transition of Eu^{3+}. The respective graphs are shown in Fig. 5(g)–(i). Here, a lower maximum S_r value of 1.94% K^{-1} at 40 K was observed. The uncertainty was below 0.4 K for the whole studied temperature range. Cycle tests indicate that the material shows a stability of 98% (Fig. S4 in the SI). These results show that both the Tb/Eu and HfO_2/Eu ratios can be used for nanothermometry with HfO_2:Eu^{3+},Tb^{3+} nanocrystals in the cryogenic region. Although combined stability measurements under repeated thermal cycling and magnetic field conditions would provide valuable insights for the potential superconducting applications, such experiments require specialized setups that allow simultaneous control of both environments and, to our acknowledge, have so far been realized only by a few research groups.[58,59] These combined measurements are crucial for future studies aimed at evaluating the long-term stability of the material under coupled external stimuli.

To better understand the operating dynamics of our nanothermometers, time-resolved photoluminescence spectroscopy measurements were performed on HfO_2:Eu^{3+},Tb^{3+} powder in the 20–100 K temperature range (Fig. 6). Fig. 6(a) and (b) show the time-resolved photoluminescence obtained when monitoring the Tb^{3+} $^5D_4 \rightarrow {}^7F_5$ (543 nm) and the Eu^{3+} $^5D_0 \rightarrow {}^7F_2$ (613 nm) emissions, respectively. The data points for both transitions could be fitted as a biexponential decay, although the Tb^{3+} decay indicates a more complex profile at longer timescales (6–10 ms), likely due to an Tb^{3+}–Eu^{3+} interaction. Fig. 6(c) shows the average lifetime values (τ_{avg}) obtained by eqn (5). First, the non-monotonic behavior of the nanomaterial at 20 and 30 K is again observed. Both steady-state and time-resolved photoluminescence experiments were repeated for this sample, and the same result was obtained. It is therefore assumed that this is an intrinsic behavior of the HfO_2:Eu^{3+},Tb^{3+} nanocrystals, which will be discussed later. After excluding these two data points, a rising Eu^{3+} average lifetime with temperature is observed, at least until 80 K, while the Tb^{3+} lifetime remained constant throughout the measured range. These results indicate a temperature-dependent $Tb^{3+} \rightarrow Eu^{3+}$ energy transfer process, which is partly responsible for the thermometric features of the HfO_2:Eu^{3+},Tb^{3+} nanocrystals. It is worth remembering that the Tb^{3+} lifetime, being monitored at 543 nm, also contains information from the HfO_2 broad emission band, which arises from defects within the doped nanocrystal rather than from a host bandgap emission (E_{gap} = 5.7 eV).[60] The intensity of this host emission is strongly dependent on the temperature (Fig. 5), supporting the hypothesis of a defect-related emission, as the release of trapped charge carriers into the valence and conduction bands (and subsequent radiative recombination) is governed by a Boltzmann distribution.[61]

$$\tau_{avg} = \frac{A_1\tau_1^2 + A_2\tau_2^2}{A_1\tau_1 + A_2\tau_2} \quad (5)$$

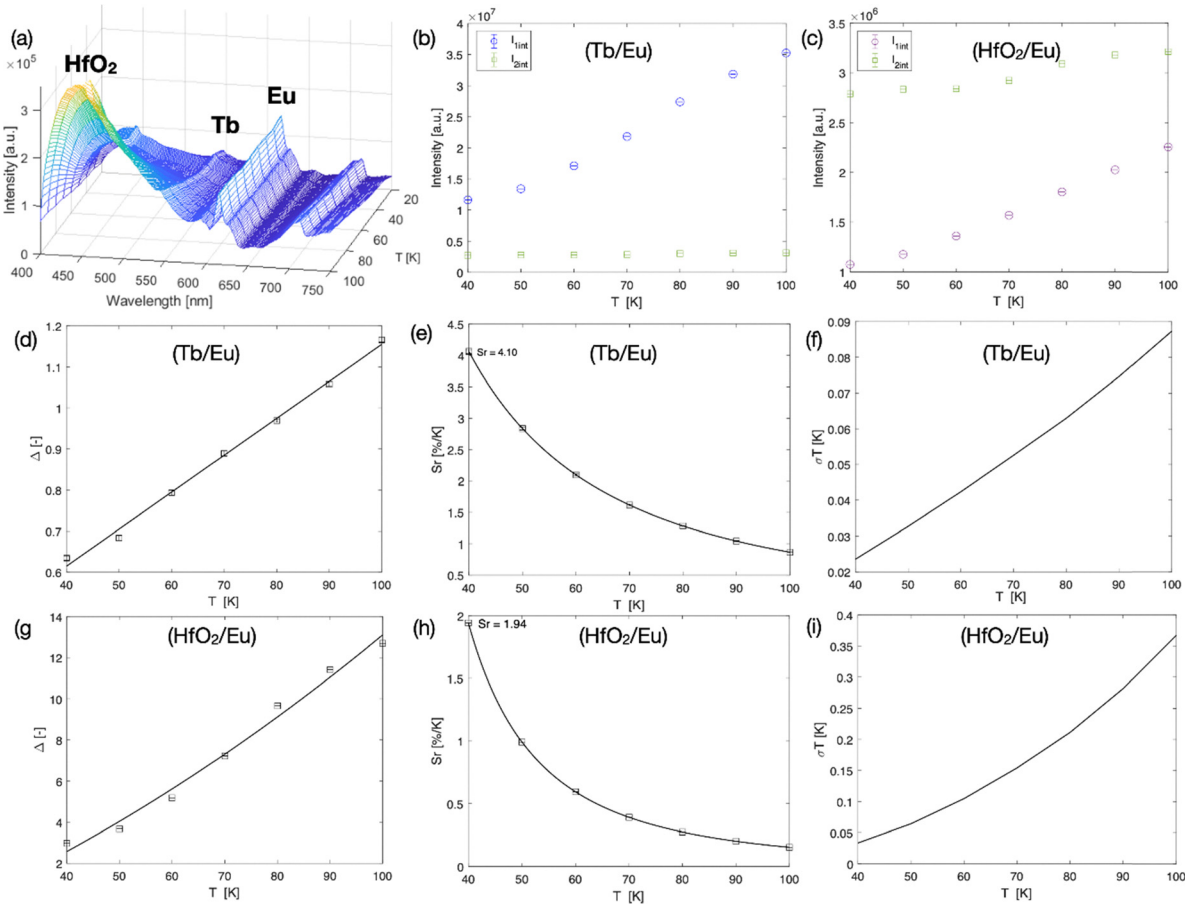

Fig. 5 Thermometry assessment for HfO_2:Eu^{3+},Tb^{3+} nanocrystals: (a) Emission map recorded at 40–100 K upon 250 nm excitation; (b) integrated emission areas as a function of temperature – blue circles represent the Tb^{3+} $^5D_4 \rightarrow {}^7F_5$ emission (centered around 545 nm) and the green squares represent the Eu^{3+} $^5D_0 \rightarrow {}^7F_2$ emission (centered around 613 nm); (c) integrated emission areas as a function of temperature – purple circles represent broad emission band from the HfO_2 host and the green squares represent the Eu^{3+} $^5D_0 \rightarrow {}^7F_2$ emission (centered around 613 nm); (d) luminescence intensity ratio Δ for the Tb:Eu electronic transitions (points show the experimental Δ parameters, and the solid line shows the best fit of the experimental points using eqn (1) (first-degree polynomial R^2 = 0.999); (e) the respective relative sensitivity S_r; (f) the respective temperature uncertainty σT (<0.09 K throughout the whole studied temperature range); (g) luminescence intensity ratio Δ for the HfO_2:Eu emissions (points show the experimental Δ parameters, and the solid line shows the best fit of the experimental points using eqn (1) (second-degree polynomial R^2 = 0.999); (h) the respective relative sensitivity S_r; (i) the respective temperature uncertainty σT (<0.4 K throughout the whole studied temperature range).

As the goal of this work was to introduce the HfO_2:Eu^{3+},Tb^{3+} nanothermometers into a coated conductor, the HfO_2:Eu^{3+},Tb^{3+} nanocrystals were deposited as a thin film on the protective layer of a coated conductor using a spin-coating technique. The respective emission spectrum of HfO_2:Eu^{3+},Tb^{3+} measured at RT as a thin film is shown in Fig. S5 in the SI. The BF-STEM image (Fig. 7(a)) shows an overview of the commercial YBCO tape, where a 60 ± 10 nm-thick HfO_2:Eu^{3+},Tb^{3+} film is deposited on a 1 μm-thick Ag protective layer. This dense thin film contains a uniform distribution of only doped HfO_2 nanocrystals, as shown *via* EDX analysis (Fig. S6 in the SI). This deposition method of the HfO_2:Eu^{3+},Tb^{3+} nanothermometric film preserves the superconducting properties, as the critical current density (J_c) of 2.0 MA cm^{-2} in self-field at 77 K remains unchanged before and after deposition.

Finally, the thermometric properties of the deposited HfO_2:Eu^{3+},Tb^{3+} thin film were evaluated in detail (Fig. 8). A general decrease in the emission intensity is observed upon incorporating the HfO_2:Eu^{3+},Tb^{3+} nanocrystals into the thin film. As shown in the emission map (Fig. 8(a)), the 545 nm peak of Tb^{3+} is no longer visible in this sample as it overlaps with the broad emission band of the HfO_2 host. Therefore, only the HfO_2/Eu ratio was employed for thermometric evaluation. We can clearly see from comparing the emission maps of the HfO_2:Eu^{3+},Tb^{3+} powder (Fig. 5(a)) and the deposited HfO_2:Eu^{3+},Tb^{3+} thin film (Fig. 8(a)) that the HfO_2/Eu intensity ratio differs and the thermometric performance is altered for the HfO_2:Eu^{3+},Tb^{3+} nanocrystals after deposition. This change in the luminescence properties can be linked to reduced surface quenching effects in the nanocrystals after deposition as thin films. As individual HfO_2:Eu^{3+},Tb^{3+} nanocrystals of ~6 nm in size, the high surface-to-volume ratio leads to a high number of surface defects, as well as a higher probability of Ln^{3+} dopants close to the surface. After being deposited as a HfO_2:Eu^{3+},Tb^{3+} thin film, the

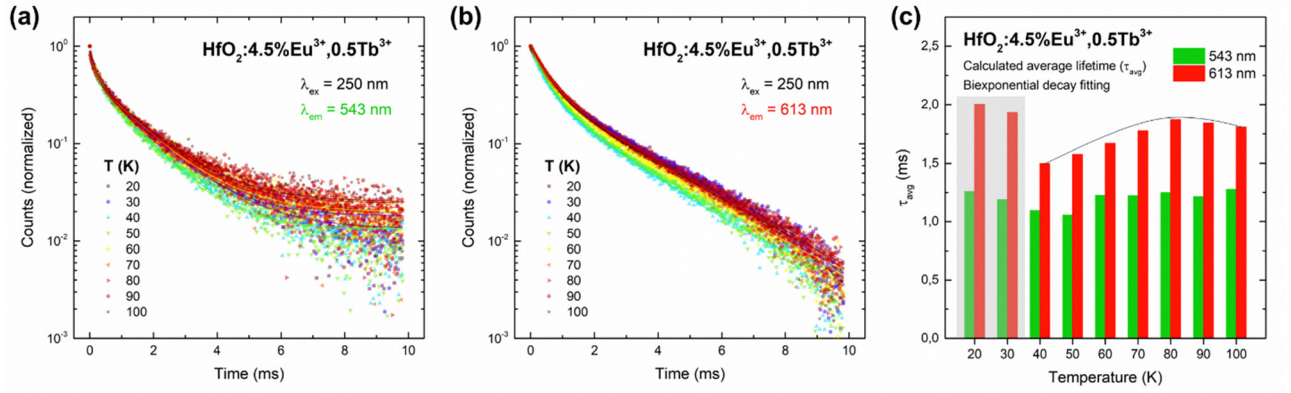

Fig. 6 Time-resolved photoluminescence spectroscopy (λ_{ex} = 250 nm) of HfO_2:4.5%Eu^{3+},0.5%Tb^{3+} nanocrystals, registered in powder form under the 20–100 K temperature range: (a) monitoring the Tb^{3+} $^5D_4 \rightarrow {}^7F_5$ emission at 543 nm; (b) monitoring the Eu^{3+} $^5D_0 \rightarrow {}^7F_2$ emission at 613 nm; (c) average lifetime values (τ_{avg}) obtained by eqn (5), in which τ_1 and τ_2 are the two time components retrieved by a biexponential decay fitting $y = y_0 + A_1e^{-x/\tau_1} + A_2e^{-t/\tau_2}$ (solid lines in Fig. 6(a) and (b)) of the experimental data points (symbols in Fig. 6(a) and (b)).

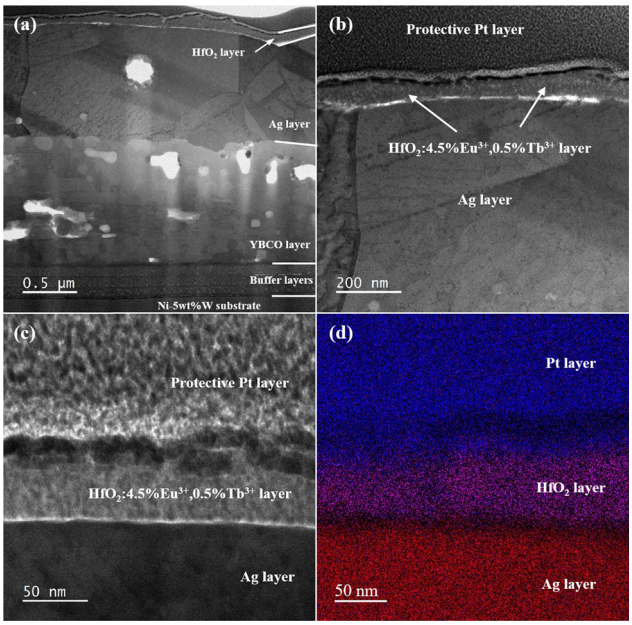

Fig. 7 Cross-sectional BF-STEM image of (a) a commercial YBCO tape with 60 ± 10 nm HfO_2:Eu^{3+},Tb^{3+} nanocrystals deposited on the top of the Ag protective layer at low magnification; (b) and (c) close-up BF-STEM images and its combined EDX maps (d) of the interface between the HfO_2:Eu^{3+},Tb^{3+} nanocrystals and the Ag protective layer. The holes in the YBCO superconducting film are due to the thinning of the TEM lamella.

nanocrystals will be densely packed on top of the coated conductor tape, isolating the Ln3+ ions from the surface. As shown in Fig. 8(b), the Eu^{3+} peak remains almost at the same intensity, whereas the intensity of the host material band increases with temperature. It can also be observed that the Tb^{3+} peak emission is very low after spin-coating, as it is mostly overlapped by the HfO_2 broadband. This is a consequence of the broadening of the HfO_2 band upon incorporation into a thin film, most likely an effect of environmental change, *i.e.*, different defect energies within the host bandgap structure. This feature could also explain the monotonic behavior now observed for the Eu^{3+} emission over the whole temperature range, contrasting with the behavior observed at 20 and 30 K for the individual HfO_2:Eu^{3+},Tb^{3+} nanocrystals. Fig. 8(c)–(e) show the thermometric parameters Δ, S_r, and σT, respectively, calculated based on the integrated areas under the curve for the HfO_2 broad emission band and the Eu^{3+} $^5D_0 \rightarrow {}^7F_2$ emission. Here, the highest S_r was obtained at 20 K and was calculated as 13.51% K^{-1}. The temperature uncertainty σT was slightly higher than that of the nanocrystals but remained below 1.1 K across the whole studied temperature range. This increase in σT is expected considering a lower overall emission signal and therefore a lower signal to noise ratio was observed. Nevertheless, these results show that the HfO_2:Eu^{3+},Tb^{3+} thin film shows excellent thermometric properties at very low temperatures.

Conclusion

In this work, luminescent HfO_2:Eu^{3+},Tb^{3+} nanocrystals were synthesized *via* a microwave-assisted solvothermal method and were characterized extensively. Doping HfO_2 nanocrystals with Eu^{3+} and Tb^{3+} ions does not significantly affect the size or shape of the nanocrystals at a total doping percentage of 5%. The optimal doping concentration for the best luminescent properties of HfO_2:Eu^{3+},Tb^{3+} nanocrystals was found to be 4.5%Eu^{3+},0.5%Tb^{3+}, resulting in a highly sensitive, cryogenic-compatible luminescent nanothermometry system with a relative sensitivity of 4.10% K^{-1} at 40 K. These nanocrystals were spin-coated on top of a coated YBCO conductor to be used as a built-in thermometry system for quench detection. The thickness of the spin-coated thin film was 60 ± 10 nm and the relative sensitivity of this system reached 13.51% K^{-1} at 20 K. Therefore, these HfO_2:Eu^{3+},Tb^{3+} nanocrystals, deposited as a thin film, can be used as a novel quench detection method, while still retaining the superconducting properties of the commercially coated conductor.

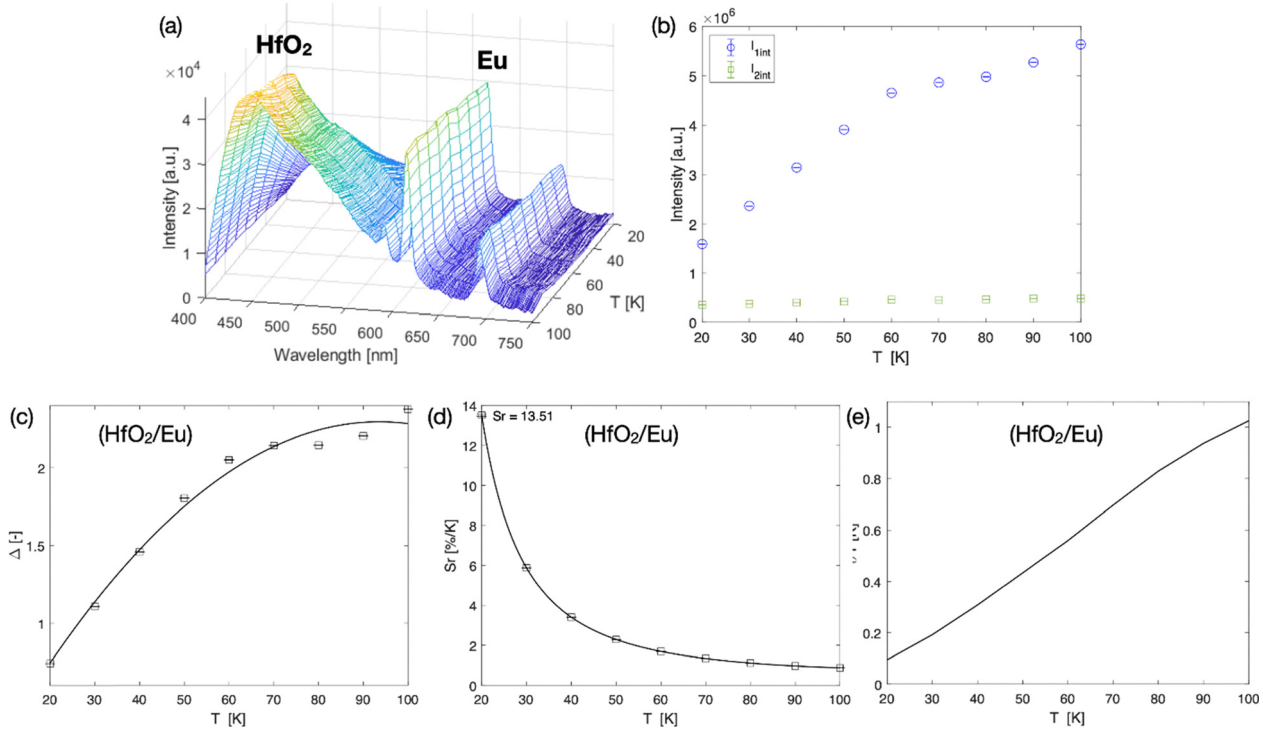

Fig. 8 Thermometry graphs for the HfO_2:Eu^{3+},Tb^{3+} thin film. (a) Emission map recorded at 20–100 K (upon 271 nm excitation). (b) Integrated emission areas as a function of temperature – blue circles represent a broad emission band from the HfO_2 host and the green squares represent the Eu^{3+} $^5D_0 \rightarrow {}^7F_2$ emission (centered around 613 nm); (c) luminescence intensity ratio Δ for the HfO_2:Eu electronic transitions (points show the experimental Δ parameters, and the solid line shows the best fit of the experimental points using eqn (1) (second-degree polynomial $R^2 = 0.999$); (d) relative sensitivity S_r; (e) temperature uncertainty $\sigma T < 1.1$ K throughout the whole studied temperature range.

Author contributions

Pauline Rooms: writing – original draft, visualization, data curation, validation, methology. Mirijam Lederer: writing – review & editing, investigation, formal analysis, data curation. Ian Pompermayer Machado: writing – review & editing, investigation, formal analysis, data curation. Martina Tsvetanova: investigation, formal analysis, data curation. Klaartje De Buysser: resources, funding acquisition. Anna M. Kaczmarek: writing – review & editing, supervision, resources, funding acquisition, conceptualization. Hannes Rijckaert: writing – review & editing, visualization, data curation, investigation, supervision, resources, project administration, conceptualization.

Conflicts of interest

There are no conflicts of interest to declare.

Data availability

The data underlying this study are available in Zenodo at https://doi.org/10.5281/zenodo.12759557 and can be accessed freely.

The supporting data for this article have been included in the supplementary information (SI). Supplementary information contains the comparison of normalized photoluminescence spectra and overview of the screening process of HfO_2:Eu^{3+},Tb^{3+} nanocrystals with different doping percentages, HAADF-STEM with corresponding EDX maps and cycle test of HfO_2:4.5%Eu^{3+}, 0.5%Tb^{3+} nanocrystals, emission spectrum and HAAFD-STEM with corresponding EDX maps of HfO_2:4.5%Eu^{3+},0.5%Tb^{3+} as thin film. See DOI: https://doi.org/10.1039/d5tc02913a.

Acknowledgements

H. R. acknowledges support and funding from the Research Foundation – Flanders (FWO) as a postdoctoral fellow in fundamental research under grant number 1280025N. This work is part of a project that has received funding from the European Research Council (ERC) under the European Union's Horizon 2020 research and innovation programme (Grant agreement No. 945945; acknowledged by A. M. K., I. P. M., and M. L.). The authors thank Dr Pablo Cayado (University of Oviedo) for scientific discussions, Célia Lucas (University of Geneva) for characterizing the superconducting properties, and Laura Van Bossele (Ghent University) for performing the PXRD measurements. Fig. 1 was created using https://BioRender.com.

References

1 J. L. MacManus-Driscoll and S. C. Wimbush, Processing and application of high-temperature superconducting coated conductors, *Nat. Rev. Mater.*, 2021, **6**, 587–604, DOI: 10.1038/s41578-021-00290-3.

2 A. Molodyk and D. C. Larbalestier, The prospects of high-temperature superconductors, *Science*, 2023, **380**(6651), 1220–1222, DOI: 10.1126/science.abq4137.
3 A. A. Armenio, *et al.*, Stability measurements on YBCO coated conductors, *IEEE Trans. Appl. Supercond.*, 2008, **18**(2), 1293–1296, DOI: 10.1109/TASC.2008.920835.
4 H. Song and J. Schwartz, Stability and Quench Behavior of $YBa_2uC_u3O_{7-x}$ Coated Conductor at 4.2 K, Self-Field, *IEEE Trans. Appl. Supercond.*, 2009, **19**(5), 3735–3743, DOI: 10.1109/TASC.2009.2023674.
5 C. Lacroix, *et al.*, Normal zone propagation in various REBCO tape architectures, *Supercond. Sci. Technol.*, 2022, **35**(5), 055009, DOI: 10.1088/1361-6668/ac56ff.
6 F. Trillaud, *et al.*, Normal zone propagation experiments on HTS composite conductors, *Cryogenics*, 2003, **43**(3–5), 271–279, DOI: 10.1016/S0011-2275(03)00044-4.
7 R. Grabovickic, *et al.*, Measurements of temperature dependence of the stability and quench propagation of a 20-cm-long RABiTS Y-Ba-Cu-O tape, *IEEE Trans. Appl. Supercond.*, 2003, **13**(2), 1726–1730, DOI: 10.1109/TASC.2003.812874.
8 O. Haugen, *et al.*, High resolution thermal imaging of hot-spots in superconducting films, *IEEE Trans. Appl. Supercond.*, 2007, **17**(2), 3215–3218, DOI: 10.1109/TASC.2007.899341.
9 G. Iannone, *et al.*, Quench propagation in commercial REBCO composite tapes, *Cryogenics*, 2020, **109**, 103116, DOI: 10.1016/j.cryogenics.2020.103116.
10 M. Marchevsky, Quench detection and protection for high-temperature superconductor accelerator magnets, *Instruments*, 2021, **5**(3), 27, DOI: 10.3390/instruments5030027.
11 R. Gyuráki, F. Sirois and F. Grilli, High-speed fluorescent thermal imaging of quench propagation in high temperature superconductor tapes, *Supercond. Sci. Technol.*, 2018, **31**(3), 034003, DOI: 10.1088/1361-6668/aaa703.
12 R. Gyuráki, *et al.*, Fluorescent thermal imaging of a non-insulated pancake coil wound from high temperature superconductor tape, *Supercond. Sci. Technol.*, 2019, **32**(10), 105006, DOI: 10.1088/1361-6668/ab38f2.
13 H. Song, M. W. Davidson and J. Schwartz, Dynamic magneto-optical imaging of transport current redistribution and normal zone propagationin $YBa_2Cu_3O_{7-\delta}$ coated conductor, *Supercond. Sci. Technol.*, 2009, **22**(6), 062001, DOI: 10.1088/0953-2048/22/6/062001.
14 S. Hasegawa, *et al.*, Quench Detection in Insulated, NI, and MI (RE)$Ba_2Cu_3O_{7-x}$ Coils With Superconducting Quench Detectors, *IEEE Trans. Appl. Supercond.*, 2024, **34**(6), DOI: 10.1109/TASC.2024.3404812.
15 X. Su, *et al.*, Visualization investigation of the full-field temperature of the damaged YBCO CC after quenching in liquid nitrogen based on bubbles distribution, *Int. J. Heat Mass Transfer*, 2024, **223**, 125283, DOI: 10.1016/j.ijheatmasstransfer.2024.125283.
16 J. Deng, *et al.*, Investigation of current and temperature distribution during quench in YBCO CC: direct observation and numerical simulation, *Supercond. Sci. Technol.*, 2025, **38**(5), 055026, DOI: 10.1088/1361-6668/add422.
17 J. Zhou, W. K. Chan and J. Schwartz, Quench Detection Criteria for $YBa_2Cu_3O_{7-\delta}$ Coils Monitored via a Distributed Temperature Sensor for 77 K Cases, *IEEE Trans. Appl. Supercond.*, 2018, **28**(5), 1–12, DOI: 10.1109/TASC.2018.2815920.
18 D. Jaque and F. Vetrone, Luminescence nanothermometry, *Nanoscale*, 2012, **4**(15), 4301–4326, DOI: 10.1039/C2NR30764B.
19 M. Dramićanin, *Luminescence thermometry: methods, materials, and applications*, Woodhead Publishing, 2018.
20 A. Bednarkiewicz, *et al.*, Standardizing luminescence nanothermometry for biomedical applications, *Nanoscale*, 2020, **12**(27), 14405–14421, DOI: 10.1039/D0NR03568H.
21 M. Quintanilla and L. M. Liz-Marzan, Guiding rules for selecting a nanothermometer, *Nano Today*, 2018, **19**, 126–145, DOI: 10.1016/j.nantod.2018.02.012.
22 S. Premcheska, M. Lederer and A. M. Kaczmarek, The importance, status, and perspectives of hybrid lanthanide-doped upconversion nanothermometers for theranostics, *ChemComm*, 2022, **58**(27), 4288–4307, DOI: 10.1039/D1CC07164E.
23 M. Suta and A. Meijerink, A theoretical framework for ratiometric single ion luminescent thermometers—thermodynamic and kinetic guidelines for optimized performance, *Adv. Theor. Simul.*, 2020, **3**(12), 2000176, DOI: 10.1002/adts.202000176.
24 A. Bednarkiewicz, *et al.*, Luminescence based temperature bio-imaging: Status, challenges, and perspectives, *Appl. Phys. Rev.*, 2021, **8**, 011317, DOI: 10.1063/5.0030295.
25 T. P. Van Swieten, A. Meijerink and F. T. Rabouw, Impact of noise and background on measurement uncertainties in luminescence thermometry, *ACS Photonics*, 2022, **9**(4), 1366–1374, DOI: 10.1021/acsphotonics.2c00039.
26 Z. Li, *et al.*, Photothermal lanthanide nanomaterials: From fundamentals to theranostic applications, *BMEMat*, 2024, **2**(4), e12088, DOI: 10.1002/bmm2.12088.
27 B. R. Anne, *et al.*, Review on electrodeposited Ni–W based composite coatings in high-temperature applications concerning oxidation behavior, *Met. Mater. Int.*, 2024, **30**(6), 1441–1458, DOI: 10.1007/s12540-023-01609-1.
28 L. Marciniak, K. Prorok and A. Bednarkiewicz, Size dependent sensitivity of Yb^{3+}, Er^{3+} up-converting luminescent nanothermometers, *J. Mater. Chem. C*, 2017, **5**(31), 7890–7897, DOI: 10.1039/C7TC02322G.
29 A. Lauria, *et al.*, Multifunctional role of rare earth doping in optical materials: Nonaqueous sol–gel synthesis of stabilized cubic HfO_2 luminescent nanoparticles, *ACS Nano*, 2013, **7**(8), 7041–7052, DOI: 10.1021/nn402357s.
30 M. Ren, *et al.*, A cryogenic luminescent ratiometric thermometer based on a lanthanide phosphonate dimer, *J. Mater. Chem. C*, 2015, **3**(33), 8480–8484, DOI: 10.1021/ja512745y.
31 X. Liu, *et al.*, Mixed-lanthanoid metal–organic framework for ratiometric cryogenic temperature sensing, *Inorg. Chem.*, 2015, **54**(23), 11323–11329, DOI: 10.1021/acs.inorgchem.5b01924.
32 A. M. Kaczmarek, Eu^{3+}/Tb^{3+} and Dy^{3+} POM@ MOFs and 2D coordination polymers based on pyridine-2, 6-dicarboxylic acid for ratiometric optical temperature sensing, *J. Mater. Chem. C*, 2018, **6**(22), 5916–5925, DOI: 10.1039/C8TC01062E.
33 A. Kaczmarek, *et al.*, Cryogenic luminescent thermometers based on multinuclear Eu^{3+}/Tb^{3+} mixed lanthanide polyoxometalates, *Dalton Trans.*, 2017, **46**(18), 5781–5785, DOI: 10.1039/C7DT01058C.

34 A. Souza and M. C. Dos Santos, The J-mixing effect in Ln^{3+} ions crystal field levels, *Chem. Phys. Lett.*, 2012, **521**, 138–141, DOI: 10.1016/j.cplett.2011.10.060.

35 C. Matuszewska and L. Marciniak, The influence of host material on NIR II and NIR III emitting Ni^{2+}-based luminescent thermometers in $ATiO_3$: Ni^{2+} (A= Sr, Ca, Mg, Ba) nanocrystals, *J. Lumin.*, 2020, **223**, 117221, DOI: 10.1016/j.jlumin.2020.117221.

36 L. R. Gerken, *et al.*, Lanthanide-doped hafnia nanoparticles for multimodal theranostics: Tailoring the physicochemical properties and interactions with biological entities, *ACS Appl. Mater. Interfaces*, 2018, **11**(1), 437–448, DOI: 10.1021/acsami.8b20334.

37 L. Deblock, *et al.*, Mapping out the aqueous surface chemistry of metal oxide nanocrystals: Carboxylate, phosphonate, and catecholate ligands, *JACS Au*, 2022, **2**(3), 711–722, DOI: 10.1021/jacsau.1c00565.

38 W. A. Mohamed, *et al.*, Lanthanide-Doped Bismuth MOFs for Tunable White Light Emission and Ratiometric Cryogenic Thermometry, *Adv. Opt. Mater.*, 2025, e03221, DOI: 10.1002/adom.202403221.

39 B. Harrington, *et al.*, Luminescence thermometry beyond the biological realm, *ACS Nanosci. Au*, 2023, **4**(1), 30–61, DOI: 10.1021/acsnanoscienceau.3c00051.

40 H. Wang, *et al.*, Enhancing Thermal Sensitivity of NIR-IIb Lanthanide Nanothermometers for In Vivo Luminescence Nanothermometry via Erbium Sublattice-Mediated Energy Recycling, *Adv. Funct. Mater.*, 2025, e06126, DOI: 10.1002/adfm.202506126.

41 E. Carrasco, *et al.*, Intratumoral thermal reading during photo-thermal therapy by multifunctional fluorescent nanoparticles, *Adv. Funct. Mater.*, 2015, **25**(4), 615–626, DOI: 10.1002/adfm.201403653.

42 C. D. Brites, S. Balabhadra and L. D. Carlos, Lanthanide-based thermometers: at the cutting-edge of luminescence thermometry, *Adv. Opt. Mater.*, 2019, **7**(5), 1801239, DOI: 10.1002/adom.201801239.

43 B. Harrington, *et al.*, Luminescence Thermometry Beyond the Biological Realm, *ACS Nanosci. Au*, 2024, **4**(1), 30–61, DOI: 10.1021/acsnanoscienceau.3c00051.

44 I. N'Dala-Louika, *et al.*, Ratiometric mixed Eu–Tb metal–organic framework as a new cryogenic luminescent thermometer, *J. Mater. Chem. C*, 2017, **5**(42), 10933–10937, DOI: 10.1039/C7TC03223D.

45 J. Horton and A. Donald, Gelation in a Synthetic Polypeptide System, in Food Polymers, *Gels and Colloids*. 1991, Elsevier. 508–512.

46 D. Baranov, *et al.*, Purification of oleylamine for materials synthesis and spectroscopic diagnostics for trans isomers, *Chem. Mater.*, 2019, **31**(4), 1223–1230, DOI: 10.1021/acs.chemmater.8b04198.

47 J. Díez-Sierra, *et al.*, All-chemical $YBa_2Cu_3O_{7-\delta}$ coated conductors with preformed $BaHfO_3$ and $BaZrO_3$ nanocrystals on Ni5W technical substrate at the industrial scale, *Supercond. Sci. Technol.*, 2021, **34**(11), 114001, DOI: 10.1088/1361-6668/ac2495.

48 E. Goossens, *et al.*, From Corrosion Casting to Virtual Dissection: Contrast-Enhanced Vascular Imaging using Hafnium Oxide Nanocrystals, *Small Methods*, 2024, **8**(10), e2301499, DOI: 10.1002/smtd.202301499.

49 L. Manxzer, *et al.*, 31. Tetragtdrfuran Complexes of Selected Early Transition Metals, *Inorg. Synth.*, 1982, **21**, 135–140, DOI: 10.1002/9780470132524.ch31.

50 J. Buha, *et al.*, Solvothermal and surfactant-free synthesis of crystalline Nb_2O_5, Ta_2O_5, HfO_2, and Co-doped HfO_2 nanoparticles, *Phys. Chem. Chem. Phys.*, 2010, **12**(47), 15537–15543, DOI: 10.1039/C0CP01298J.

51 J. De Roo, *et al.*, Fast, microwave-assisted synthesis of monodisperse HfO_2 nanoparticles, *J. Nanopart. Res.*, 2013, **15**(7), 1778, DOI: 10.1007/s11051-013-1778-z.

52 H. Rijckaert, Preparation of the S/TEM Lamella of Commercial $REBa_2Cu_3O_{7-x}$ Coated Conductors by FIB, *IEEE Trans. Appl. Supercond.*, 2024, **34**(7), DOI: 10.1109/TASC.2024.3438690.

53 A. M. Kaczmarek, R. Van Deun and M. K. Kaczmarek, TeSen–tool for determining thermometric parameters in ratiometric optical thermometry, *Sens. Actuators, B*, 2018, **273**, 696–702, DOI: 10.1016/j.snb.2018.06.086.

54 Y. Cui, *et al.*, A luminescent mixed-lanthanide metal–organic framework thermometer, *J. Am. Chem. Soc.*, 2012, **134**(9), 3979–3982, DOI: 10.1021/ja2108036.

55 Z. Wang, *et al.*, Lanthanide–organic framework nanothermometers prepared by spray-drying, *Adv. Funct. Mater.*, 2015, **25**(19), 2824–2830, DOI: 10.1002/adfm.201500518.

56 D. Ananias, *et al.*, Photoluminescent thermometer based on a phase-transition lanthanide silicate with unusual structural disorder, *J. Am. Chem. Soc.*, 2015, **137**(8), 3051–3058, DOI: 10.1021/ja512745y.

57 A. M. Kaczmarek, *et al.*, Luminescent ratiometric thermometers based on a 4f–3d grafted covalent organic framework to locally measure temperature gradients during catalytic reactions, *Angew. Chem., Int. Ed.*, 2021, **60**(7), 3727–3736, DOI: 10.1002/anie.202013377.

58 M. Aragon-Alberti, *et al.*, Rethinking Assumptions: Assessing the Impact of Strong Magnetic Fields on Luminescence Thermometry, *J. Am. Chem. Soc.*, 2024, **146**(49), 33723–33731, DOI: 10.1021/jacs.4c11584.

59 D. A. Gálico and M. Murugesu, Magneto-Luminescence Thermometry with Magnetic Circularly Polarized Luminescence, *Angew. Chem., Int. Ed.*, 2025, **64**(35), e202505806, DOI: 10.1002/anie.202505806.

60 E. Bersch, *et al.*, Band offsets of ultrathin high-κ oxide films with Si, *Phys. Rev. B: Condens. Matter Mater. Phys.*, 2008, **78**(8), 085114, DOI: 10.1103/PhysRevB.78.085114.

61 E. Montes, *et al.*, Effect of europium concentration on the photoluminescent and thermoluminescent properties of HfO_2: Eu^{3+} nanocrystals, *Ceram. Int.*, 2018, **44**(7), 8081–8086, DOI: 10.1016/j.ceramint.2018.01.250.